Effect of Transport and Reaction on the Shape Evolution of Cavities during Wet Chemical Etching

Chee Burm Shin and Demetre J. Economou*

Department of Chemical Engineering, University of Houston, Houston, Texas 77204-4792

ABSTRACT

The effect of fluid flow, transport, and reaction on the shape evolution of two-dimensional cavities during wet chemical etching was studied. Finite element methods were employed to solve for the fluid velocity profiles and for the etchant concentration distribution in cavities of arbitrary shape. A moving boundary scheme was developed to track the shape evolution of the etching cavity. In the case of pure diffusion and under mass-transfer control, a mask with finite thickness resulted in significantly better etch factor (etch anisotropy) as compared to an infinitely thin mask, albeit the etch rate was essentially unaffected. With fluid flow past the cavity, the etch rate increased fourfold and the etch factor increased by 40% as compared to pure diffusion, under the conditions examined. In addition, the etch rate, etch factor, and cavity wall profiles showed a strong dependence on etch time as the cavity aspect ratio (depth/width) increased with time during etching.

In the modern microelectronics industry, intricate patterns are etched through resist masks into thin films of semiconductors, insulators, and metals. For example, etching patterns of controlled shape and with smooth surfaces into films of GaAs are important in the fabrication of optoelectronic devices; and etching of Cu vias is common in printed circuit board fabrication. Wet chemical methods are widely employed for etching thin and thick films ($\sim$1-100 μm). Such methods are characterized by excellent selectivity and relatively high etch rate (1, 2). Wet chemical etching is highly anisotropic when dominated by crystallographic effects; extremely high aspect ratios (40:1) in submicron structures have been obtained (3). In the absence of crystallographic effects significant mask undercut may result. However, by judicious selection of hydrodynamic conditions (4, 5) or by using photon-assisted techniques (6), mask undercut may be minimized or eliminated.

During etching some means of solution "agitation" is frequently provided, for example by directing etching fluid jets towards the surface of the workpiece. When etching is controlled by surface reaction kinetics, the shape of the resulting cavity may be predicted by geometric considerations alone, if the surface reaction rate is known for the different crystallographic orientations. However, when etching is controlled by mass transfer to or from the etching surface (e.g., when the surface reaction is very fast), the resulting cavity shape depends in a complex manner on the local fluid velocity profiles and on the concentration distribution of the reactants and/or products. Under such conditions, prediction of the shape evolution and of the final cavity wall profile is far more difficult. Mathematical models based on fundamental principles of transport and reaction phenomena may then be useful in identifying the process operating conditions which result in high etch rate with minimum mask undercut.

Vuik and Cuvelier (7) studied the shape evolution of two-dimensional etching cavities in a quiescent solution (pure diffusion with no fluid flow). The effect of surface reaction rate as compared to the diffusion rate was examined. In a series of papers, Kuiken (8-10) used asymptotic methods to derive semianalytical solutions of etching profiles in quiescent solutions and under mass-transfer control (infinitely fast surface reaction). A characteristic bulging of the profile was observed close to the mask edge (the mask was assumed to be infinitely thin). It was further shown that a similar bulging occurs even when hydrodynamic flow is imposed past the cavity. Alkire et al. (11) and Alkire and Deligianni (5) studied the effectiveness of fluid flow in rinsing the reaction products from cavities of invariant shape and of different aspect ratios.

Although the effect of fluid flow has been recognized as being important, and despite the interest in studying the shape evolution of etching cavities under fluid flow conditions, there appears to be no published work on the shape

evolution under the combined effects of fluid flow and mass transfer.

In addition to etching through masks, shape evolution phenomena are encountered in a variety of situations such as deposition through masks (12) and pitting corrosion (11). It is therefore worthwhile to develop general mathematical methods capable of tracking the shape evolution of cavities under diverse operating conditions.

In the present work a mathematical model is presented to study the effect of fluid flow, transport, and reaction on the shape evolution of two-dimensional cavities during wet chemical etching. Finite element methods were employed to solve for the fluid velocity profiles and for the concentration distribution of the etchant species in the cavity region. A moving boundary scheme was developed to track the shape evolution of the cavity during etching. The effects of fluid velocity, speed of surface reaction, and cavity aspect ratio on etch rate and etch anisotropy were studied.

Model Formulation

A schematic of the system studied is shown in Fig. 1. A solid film partially protected by an inert mask is placed in a solution which flows past the exposed film. At time zero, when the position of the film surface is at $\Gamma_6(0)$, the solution entering the cavity region through the left is assumed to contain an etchant species, which is capable of reacting with the film but is inert against the etching mask. The etchant species are transported by convection and diffusion to the film surface where they react thereby etching the film. As film etching proceeds, the cavity shape evolves with time according to the etch rate distribution along the cavity walls. The deformation of the cavity affects the local fluid flow and etchant concentration distributions which in turn affect the further shape evolution of the cavity. In Fig. 1, the moving etching surface $\Gamma_6(t)$ is shown at some
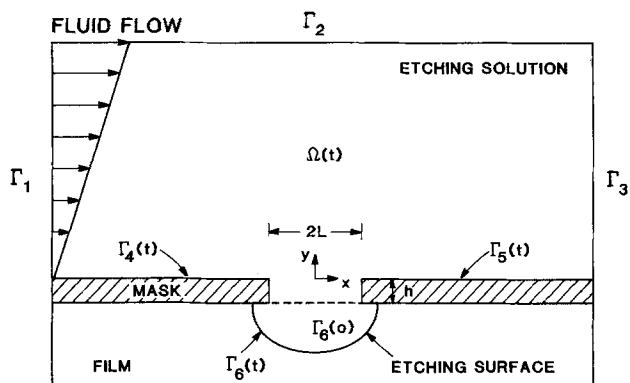

Fig. 1. Schematic of the etching system studied

*Electrochemical Society Active Member.

time t partway during etching. Because the etching solution is capable of etching in all directions, a characteristic mask undercut develops. The goal of the etching process is to minimize or totally eliminate the mask undercut while maintaining a high etch rate. A practical etching example may be that of etching GaAs using Br_2 or H_2O_2 solution (13), or that of etching Cu in an HCl solution.

Because of the microscopic dimensions of the cavity some simplifications can be made regarding the flow field. First, the relevant Reynolds number (see Eq. [15] for definition) is less than unity. Therefore, Stokes flow (or creeping flow) may be assumed to prevail in the cavity region. Second, the velocity profile close to the wall (mask) in regions far away from the cavity mouth may be assumed to be linear with a zero velocity at the wall. The additional assumptions outlined as follows simplify the mathematical analysis of the problem although the salient features of the process are preserved: (i) incompressible flow of a Newtonian fluid; (ii) isothermal system with constant physical properties; (iii) only one species in the solution is important in the etching reaction which follows linear kinetics; (iv) two-dimensional cavity, i.e., the size of the cavity in the direction normal to the paper is large compared to the other dimensions of the cavity; (v) the surface is isotropic, i.e., the etching rate constant is independent of position along the surface.

The problem is then to find the time dependent shape of the boundary $\Gamma_6(t)$. At any time during etching, the further evolution of the boundary depends on the etch rate distribution along the surface $\Gamma_6(t)$. This in turn depends on the concentration distribution in the vicinity of the moving boundary. The following equations and boundary conditions were used in order to compute the velocity and concentration fields.

The flow field was obtained by solving the Stokes equation

$$\rho \frac{\partial \mathbf{u}}{\partial t} = -\nabla p + \nabla \rho^2 \mathbf{u} \ \ \text{in} \ \Omega(t) \tag{1}$$

along with the continuity equation

$$\nabla \cdot \mathbf{u} = 0 \ \ \text{in} \ \Omega(t) \tag{2}$$

Here $\Omega(t)$ is the time dependent domain bounded by surface Γ_i, $i = 1,...,6$ as shown in Fig. 1. Surfaces Γ_1, Γ_2, and Γ_3 are fixed in time, but surfaces Γ_4, Γ_5, and Γ_6 evolve with time. The relevant boundary conditions are

$$\frac{\partial u_x}{\partial x} = 0 \ \ u_y = 0 \ \ \text{on} \ \Gamma_1 \ \text{and} \ \Gamma_3 \tag{3}$$

$$u_x = \text{const} \ \ u_y = 0 \ \ \text{on} \ \Gamma_2 \tag{4}$$

$$u_x = 0 \ \ u_y = 0 \ \ \text{on} \ \Gamma_4(t), \Gamma_5(t), \text{and} \ \Gamma_6(t) \tag{5}$$

Boundary conditions Eq. [3] and [4] imply that a shear flow prevails far to the left and far to the right of the cavity. Boundary condition Eq. [5] is the no slip condition along solid walls. The initial condition was $\mathbf{u} = \mathbf{u}_0$, where $\mathbf{u}_0$ is the velocity field at time $t = 0$ [i.e., when Γ_6 is at position $\Gamma_6(0)$].

The flow field found by solving Eq. [1] and [2] with the associated boundary conditions Eq. [3]-[5] was then used in the convective diffusion Eq. [6] below to find the two-dimensional concentration distribution of the etchant species in the cavity region

$$\frac{\partial c}{\partial t} + \mathbf{u} \cdot \nabla c = D\nabla^2 c \ \ \text{in} \ \Omega(t) \tag{6}$$

with boundary conditions

$$c = c_0 \ \ \text{on} \cdot \Gamma_1 \tag{7}$$

$$\nabla c \cdot \mathbf{n} = 0 \ \ \text{on} \ \Gamma_2, \Gamma_3, \Gamma_4(t), \text{and} \ \Gamma_5(t) \tag{8}$$

$$D\nabla c \cdot \mathbf{n} = -kc \ \ \text{on} \ \Gamma_6(t) \tag{9}$$

The initial condition was $c(t = 0) = 0$ everywhere in $\Omega(t = 0)$. Here c is the concentration of the etching species,

k is the etching (surface) reaction rate constant, and $\mathbf{n}$ is the unit normal vector pointing outwards the computational domain.

Equation [8] implies that the mask is unreactive, and Eq. [9] implies a first-order chemical reaction at the moving boundary. The movement of the boundary was described by

$$v_n = -\sigma \nabla c \cdot \mathbf{n} \tag{10}$$

where v_n is the velocity of the moving boundary $\Gamma_6(t)$ in the direction of the outward normal and σ is given by

$$\sigma = \frac{DM_s}{m\rho_s} \tag{11}$$

where M_s is the molecular weight of the solid, ρ_s is the solid density, and m is a stoichiometric coefficient in the etching reaction as shown in Eq. [12]

$$S + mE \rightarrow qP \tag{12}$$

where m moles of etchant E are consumed per mole of solid S reacting. The initial condition for Eq. [10] was that the boundary at $t = 0$ was $\Gamma_6(0)$ as shown in Fig. 1.

The governing equations, boundary, and initial conditions were nondimensionalized by introducing

$$X = x/L \ \ Y = y/L \ \ \mathbf{U} = \mathbf{u}/u_c \tag{13}$$

$$C = c/c_0 \ \ \tau = tu_c/L \ \ P = p/(\rho u_c^2) \tag{14}$$

$$\text{Re} = u_c L/\nu \ \ \text{Pe} = u_c L/D \tag{15}$$

$$\Phi = kL/D \ \ \beta = u_c L/(\sigma c_0) \ \ V_n = v_n/u_c \tag{16}$$

Here L is the half-width of the cavity mouth, and u_c is the magnitude of the flow velocity at the center of the cavity mouth (at $x = y = 0$). This velocity may be related to the shear stress at the wall (mask) far from the cavity mouth. For given etching equipment geometry and operating conditions, the wall shear stress may in turn be related to more accessible quantities such as the solution flow rate.

The dimensionless form of Eq. [1]-[5] is

$$\frac{\partial \mathbf{U}}{\partial \tau} = -\nabla P + \frac{1}{\text{Re}} \nabla^2 \mathbf{U} \ \ \text{in} \ \Omega(\tau) \tag{17}$$

$$\nabla \cdot \mathbf{U} = 0 \ \ \text{in} \ \Omega(\tau) \tag{18}$$

$$\frac{\partial U_x}{\partial x} = 0 \ \ U_y = 0 \ \ \text{on} \ \Gamma_1 \text{and} \ \Gamma_3 \tag{19}$$

$$U_x = \text{const.} \ \ U_y = 0 \ \ \text{on} \ \Gamma_2 \tag{20}$$

$$U_x = 0 \ \ U_y = 0 \ \ \text{on} \ \Gamma_4(\tau), \Gamma_5(\tau), \Gamma_6(\tau) \tag{21}$$

$$\mathbf{U} = \mathbf{U}_0 \text{ at } \tau = 0 \tag{22}$$

The dimensionless convective-diffusion equation and the associated boundary conditions read

$$\frac{\partial C}{\partial \tau} + \mathbf{U} \cdot \nabla C = \frac{1}{\text{Pe}} \nabla^2 C \ \ \text{in} \ \Omega(\tau) \tag{23}$$

$$C = 1 \ \ \text{on} \ \Gamma_1 \tag{24}$$

$$\nabla C \cdot \mathbf{n} = 0 \ \ \text{on} \ \Gamma_2, \Gamma_3, \Gamma_4(\tau), \text{and} \ \Gamma_5(\tau) \tag{25}$$

$$\nabla C \cdot \mathbf{n} = -\Phi C \ \ \text{on} \ \Gamma_6(\tau) \tag{26}$$

The initial condition was

$$C = 0 \text{ at } \tau = 0 \ \ \text{in} \ \Omega(\tau) \tag{27}$$

Finally, the dimensionless form of Eq. [10] is Eq. [28] below

$$\nabla C \cdot \mathbf{n} = -\beta V_n \tag{28}$$

Parameter Φ (Eq. [16] and [26]), the so called Thiele modulus, shows the relative importance of diffusion as compared to reaction. When $\Phi >> 1$, surface reaction is infinitely fast compared to diffusion (mass-transfer controlled case). The opposite extreme is that of $\Phi << 1$ implying a

very sluggish reaction (reaction controlled case). In the latter case the concentration of the etchant species is essentially equal to c_o throughout the cavity region. The reaction rate is then expected to be uniform along the etching surface (equal to kc_o), except when crystallographic etching plays a role, i.e., when the value of k depends on the orientation of the surface for a crystalline solid. The Peclet number, Pe, shows the relative importance of mass transport by convection as compared to diffusion. When Pe $\gg 1$, convection is the dominant mode of mass transfer.

The case of pure diffusion (no fluid flow) was examined as well. In such case the governing equation and boundary and initial conditions are, in dimensionless form

$$\frac{\partial C}{\partial T} = \nabla^2 C \text{ in } \Omega(T) \qquad [29]$$

$$C = 1 \text{ on } \Gamma_1, \Gamma_2, \text{ and } \Gamma_3 \qquad [30]$$

$$\nabla C \cdot \mathbf{n} = 0 \text{ on } \Gamma_4(T), \Gamma_5(T) \qquad [31]$$

$$\nabla C \cdot \mathbf{n} = -\Phi C \text{ on } \Gamma_6(T) \qquad [32]$$

$$\nabla C \cdot \mathbf{n} = -BV_n^* \text{ on } \Gamma_6(T) \qquad [33]$$

$$C = 1 \text{ in } \Omega(0) \qquad [34]$$

where

$$T = tD/L^2 \quad V_n^* = v_n L/D, \text{ and } B = D/(\sigma c_o) \qquad [35]$$

One notes that

$$\beta = \text{PeB} \quad V_n^* = \text{Pe}V_n \text{ and } \tau = \text{PeT} \qquad [36]$$

In addition, taking into account Eq. [36], one observes that Eq. [33] describing the movement of the boundary in the case of pure diffusion, is identical to Eq. [28] describing the movement of the boundary in the case of fluid flow.

Parameter B (and β) is a measure of the speed of the boundary movement. When B $\gg 1$ ($\beta \gg 1$), the boundary moves only very slowly. The diffusion process (or convective-diffusion for the case of β) is then rapid, and the concentration profiles can quickly relax to their steady-state value corresponding to the instantaneous position of the moving boundary. This is the so-called quasi-steady-state approximation. As an example, when etching GaAs in a HCl-H_2O_2-H_2O solution in which the etchant (H_2O_2) concentration is $1M$, the value of B = 110. One observes that the quasi-steady-state approximation may be good for practical etching systems (10, 13).

Method of Solution

The finite element method was chosen for the present problem since the method is well suited for domains of irregular shape. The computational domain and the finite element grid used are shown in Fig. 2. For the case of fluid flow, the position of boundary Γ_1 was chosen at $X = -5$, that of Γ_2 was set at $Y = 5$, and the position of Γ_3 was set at $X = 5$. The position of the moving boundary Γ_6 in this particular case corresponds to the profile shown in Fig. 5a for T = 34.7. Boundaries Γ_4, Γ_5, and Γ_6 evolve with time but boundaries Γ_1, Γ_2, and Γ_3 are stationary. Numerical experi-

ments showed that by positioning boundaries Γ_1, Γ_2, and Γ_3 further away from the cavity (compared to their position shown in Fig. 2) did not affect the results, for the range of parameter values used. Further numerical experiments were conducted to study the effect of the number of elements used. The element mesh was made denser around the mouth of the cavity and within the cavity where steeper concentration gradients are expected. In addition, enough elements were needed to ensure success of the moving boundary scheme to be described below. The total number of elements increased with time owing to element addition to accommodate the expanding boundary $\Gamma_6(t)$. For the case shown in Fig. 2, 1120 bilinear quadrilateral elements (and 1204 nodes) were used. Refining the mesh even further had no significant effect on the results, for the parameter range studied.

The solution to the moving boundary problem was obtained in a stepwise manner. Consider a time τ^n during etching, for which the position of the moving boundary X_j^n, the velocity field U^n, and the etchant concentration field C^n are known. Here the superscript n denotes the nth time step and $\tau^0 = 0$. X_j^n is the position vector of the jth node on the moving boundary $\Gamma_6(\tau^n)$. Then quantities X_j^{n+1}, U^{n+1}, and C^{n+1} were obtained through the following procedures.

1. For the time interval $\Delta\tau = \tau^{n+1} - \tau^n (n = 0, 1, \ldots)$, the etching surface was regarded as fixed. For this fixed boundary domain, Eq. [17], [18], and [23] along with the associated boundary conditions were solved by an implicit predictor-corrector scheme [14] to obtain U^{n+1} and C^{n+1}.

2. The normal unit vector $\mathbf{n}_j^n$ at point X_j^n was found by the method described in Glowinski [p. 416 of Ref. (17)].

3. The value of the etchant flux along the reactive surface $\nabla C \cdot \mathbf{n}$ was obtained as described in Glowinski [p. 398 of Ref. (17)].

4. The new position of the boundary X_j^{n+1} was then evaluated using Eq. [37] below

$$X_j^{n+1} = X_j^n + \Delta\tau \, V_n \mathbf{n}_j^n \qquad [37]$$

where V_n was found from Eq. [28] and the already calculated value of the flux $\nabla C \cdot \mathbf{n}$. A procedure identical to the one described above (substeps [1]-[4]) was then employed to locate the position of the moving boundary at the next time step τ^{n+2}. The shape evolution of the etching cavity was thus followed. Since the computational domain $\Omega(\tau)$ was expanding with time, new elements were added to the mesh inside the cavity in order to maintain a fine spatial discretization.

The finite element method and the penalty function formulation were used to obtain the velocity field. The Streamline Upwind/Petrov Galerkin (SU/PG) finite element method was used to solve for the etchant concentration field. The SU/PG method is well suited for convection-dominated problems (high Peclet numbers), such as the problem at hand. In this method, diffusion is added which, however, acts only in the flow direction. Hence, the robust qualities of the classical upwind finite element methods (e.g., upwind Galerkin finite elements) are maintained but the new method is not subject to the "artificial diffusion" criticisms associated with the classical methods. More information about the SU/PG method may be found in Ref. (15) and (16).

Equation [37] is an explicit time integration scheme for the moving boundary. An implicit scheme could also be used of the predictor-corrector type [see also Ref. (18)]. However, the computational costs would be much higher. The explicit time integration scheme was then used with time step small enough to ensure convergence and stability. Typically 100-150 time steps were used in order to compute the shape evolution of a cavity (such as shown in Fig. 5a and 8a). The magnitude of the time step was determined adaptively. Smaller time steps were used initially when the etch rate was higher. Calculations were performed on a dedicated VAX station II/RC computer. A complete shape evolution calculation under fluid flow conditions required 12-24h of CPU time depending on the conditions used.

When solving the problem of pure diffusion, the position of boundary Γ_1 was chosen at $X = -7.5$, that of Γ_2 was set

(-5,4)   (5,4)
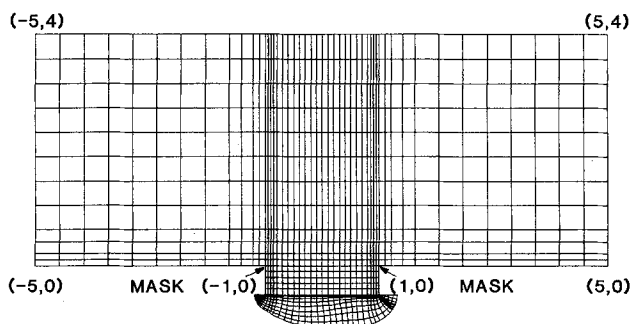
(-5,0)   MASK   (-1,0)   (1,0)   MASK   (5,0)

Fig. 2. Computational domain and finite element grid. The position of the moving boundary shown here corresponds to time T = 34.7 of Fig. 5a.
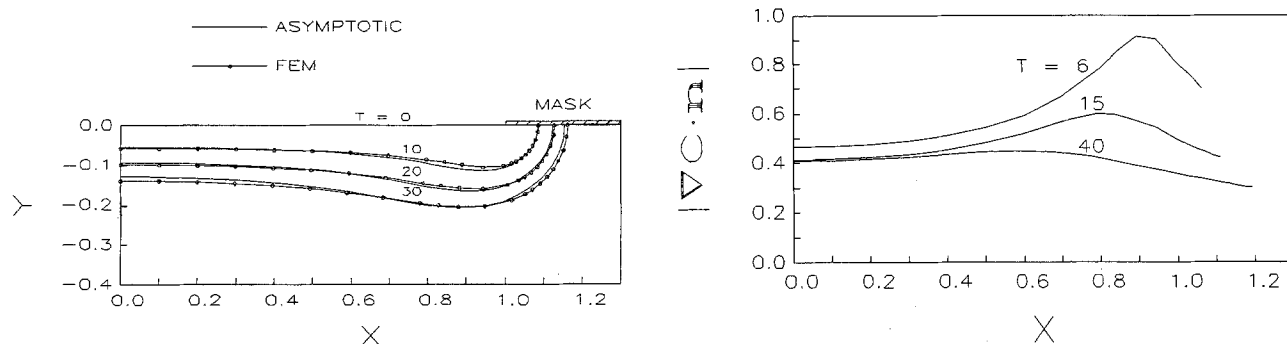
Fig. 3. (a, left) Comparison of the finite element solution (——•——) with an asymptotic solution (———) presented in Ref. (8). Quiescent solution (no fluid flow), and infinitely thin mask. Other conditions were, $\Phi \rightarrow \infty$, and B = 100. (b, right) Reactant flux (instantaneous etch rate) distribution along the reactive surface at different times during etching. Conditions were as in Fig. 3a.

at $Y = 6.5$ and the position of Γ_3 was set at $X = 7.5$. A larger domain size was used for pure diffusion as compared to forced convection because in the former case the concentration boundary layer expanded with time. When considering long etching times, an alternative is to use an asymptotic expression for the concentration far from the cavity (7). This will perhaps reduce the computational costs. Typically, 100 time steps were used for a complete shape evolution calculation (such as shown in Fig. 4). For pure diffusion the computation time was 3-5h of CPU on the VAX station II/RC computer.

Results and Discussion

In order to test the numerical code used to solve the moving boundary problem, numerical results were compared with an asymptotic solution obtained by Kuiken (8). The author examined the simplified case of etching through a slit under conditions of pure diffusion (no fluid flow), infinitely fast reaction ($\Phi \rightarrow \infty$), and infinitely thin mask. The comparison is shown in Fig. 3a where, owing to symmetry, only half of the cavity is shown. The solid lines without points are from Kuiken's asymptotic solution which is valid for long times (T >> 1) and small vertical displacements of the surface ($|Y| << 1$, where $|Y|$ is the absolute value of Y). The numerical results of the present work, shown by the solid lines with points, are in good agreement with the asymptotic solution.

The etch profiles in Fig. 3a reveal a characteristic bulging near the mask edge. This is because of higher etch rate there due to reactant diffusion from the areas above the inert mask. The bulging becomes less pronounced as the cavity deepens and the reactant diffusion path increases. The etch factor (EF), defined here as the etched depth at the center of the cavity mouth divided by the

mask undercut, is a measure of the etch anisotropy achieved. The higher the etch factor, the better the anisotropy. For perfect anisotropic etching (no mask undercut), the etch factor tends to infinity. The etch factor in Fig. 3a is less than unity at the early times (*e.g.*, EF = 0.66 at T = 10), but exceeds unity at later times (see also Fig. 10). Figure 3b shows the reactant flux distribution (*i.e.*, the instantaneous etch rate distribution) along the reactive surface for a cavity etching under the conditions of Fig. 3a. X is the *x*-coordinate of a point along the reactive boundary. The rightmost point of each curve corresponds to the point where the boundary meets the mask (undercut region). Early during etching (T = 6), the flux is much higher close to the mask edge (mask edge corresponds to $X = 1$) as compared to the cavity center ($X = 0$). This results in the characteristic bulging of the wall profiles. At later times, the flux distribution is less nonuniform. At very long times the etch rate will be uniform along the etching surface. The value of the flux decreases monotonically with time because the diffusion layer thickness increases with time.

Figure 4a shows the shape evolution of a cavity under conditions identical to those of Fig. 3 except that the mask thickness was 25% of the cavity mouth width ($h/2L = 0.25$). As in Fig. 3, only half of the cavity is shown. Compared to Fig. 3a, the bulging effect is much less pronounced, even at the initial stages of etching. This is due to the larger diffusion length of the reactant from the area above the inert mask to the etching surface. Etch anisotropy (etch factor) is enhanced using a finite thickness mask (see also Fig. 10), and etch rate is only slightly affected. The corresponding flux distribution along the etching surface is shown in Fig. 4b. Compared to Fig. 3b, the maximum in the flux at early times is much reduced. This explains the relatively weak bulging of the cavity wall profiles even at the initial stages
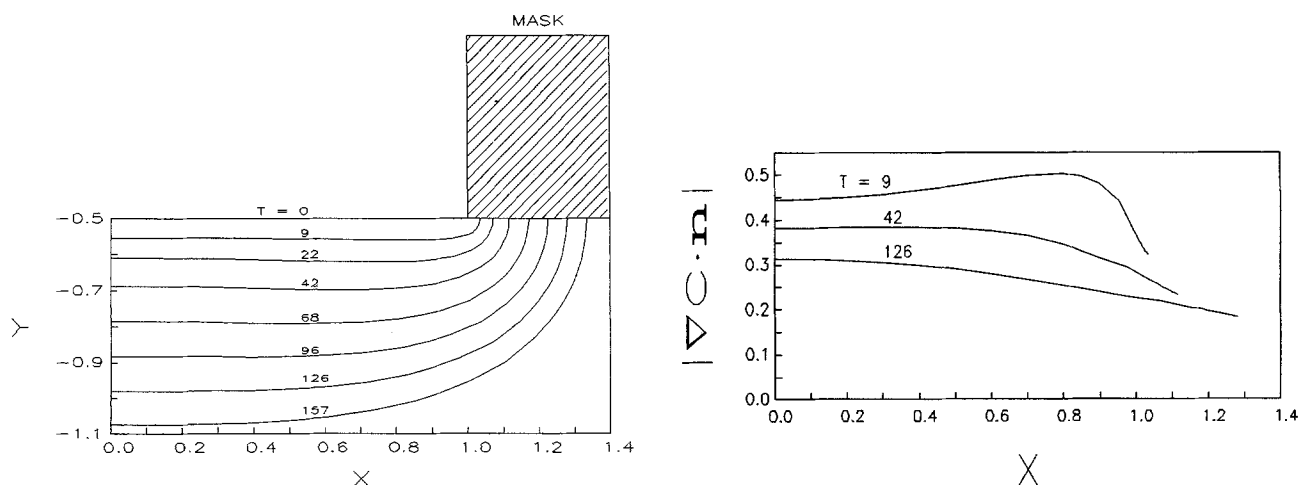

Fig. 4. (a, left) Shape evolution of a cavity in a quiescent solution. Conditions were the same as in Fig. 3a except that the mask thickness was 1/4 of the cavity mouthwidth. (b, right) Reactant flux (instantaneous etch rate) distribution along the reactive surface at different times during etching. Conditions were as in Fig. 4a.
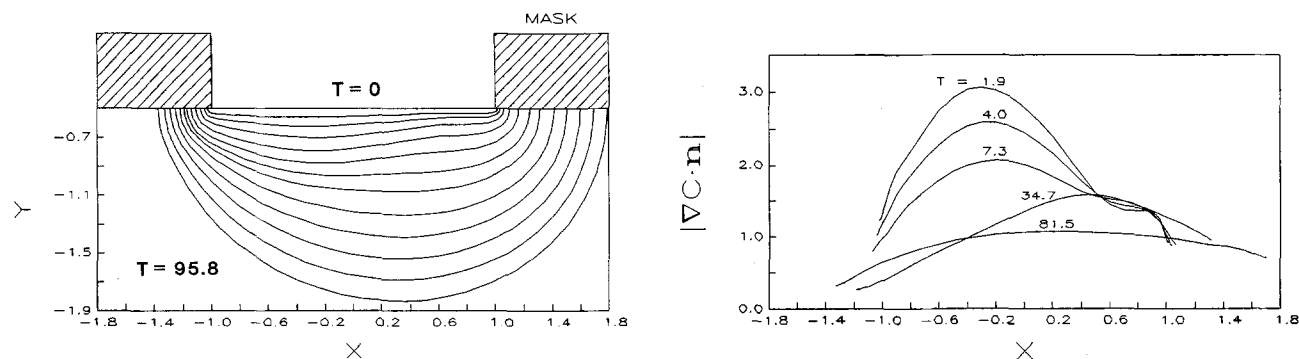
Fig. 5. (a, left) Shape evolution of a cavity under fluid flow conditions. Other conditions were Pe = 100, Re = 0.1, B = 100, and $\Phi \to \infty$. Cavity wall profiles are shown for dimensionless times T = 0, 1.9, 4.0, 7.3, 12.3, 18.8, 26.9, 34.7, 45.6, 56.7, 68.6, 81.5, and 95.8. Mask thickness was 1/4 of the cavity mouthwidth. (b, right) Reactant flux (instantaneous etch rate) distribution along the reactive surface at different times during etching. Conditions were as in Fig. 5a.

of etching. As before, flux (instantaneous etch rate) becomes less nonuniform and decreases monotonically with time.

The effect of fluid flow on the shape evolution of a cavity is depicted in Fig. 5a. Conditions were otherwise the same as in Fig. 4a except that Pe = 100 and Re = 0.1. For this case the dimensionless wall shear stress was $\tau_s L/(\mu u_c) = 6.23$, where τ_s is the wall shear stress far for the cavity mouth. The etch profiles are now asymmetric owing to fluid flow past the cavity (the fluid enters from the left). The time scale in Fig. 5 is expressed in terms of T (instead of in terms of τ), so that the etch rates obtained from Fig. 4a and 5a can be compared directly. One observes much faster etching with fluid flow as compared to pure diffusion; on the average, about four times faster under the present conditions (see also Fig. 9). Etch anisotropy is also significantly enhanced. For example, for the same etched depth of 0.58 dimensionless units (note that the cavity mouth half-width has by definition a unit length), the etch factor is 1.58 for the case of pure diffusion (Fig. 4a) but becomes 2.25 for the case of fluid flow (Fig. 5a), which amounts to 40% improvement (see also Fig. 10). Furthermore, at early times (T < 20), etching is faster to the left of the centerline X = 0, and the left mask is undercut more compared to the right mask. However, the situation reverses at later times and the etch rate and mask undercut are higher to the right of the centerline. These observations are further supported by Fig. 5b which shows the flux (instantaneous etch rate) distribution along the etching cavity walls, for several times during etching. For a particular time T, the end points of the corresponding curve show the rate of mask undercut at that time. At early times the etching rate distribution is very nonuniform with a pronounced peak to the left of the centerline. At later times the etching rate distribution becomes less nonuniform. In order to explain the observed features one needs to look closer at the hydrodynamic conditions prevailing in the cavity as the cavity aspect ratio changes during etching.

The fluid flow distribution in the cavity depends strongly on the cavity aspect ratio (depth/mouthwidth)

(5, 11, 19). For small aspect ratios (<1:3), the external flow invades the cavity, with weaker recirculating patterns developing in the corner regions. However, for large aspect ratios, the external flow is incapable of penetrating the cavity, and a large recirculating eddy develops which fills almost the entire volume of the cavity. This is shown in Fig. 6 which is a velocity vector plot of the region within the cavity. Figure 6a corresponds to the profile of Fig. 5a at T = 4.0. The cavity aspect ratio is then slightly larger than 1:4 and the penetration of the cavity by the external flow is evident. Figure 6b corresponds to the profile of Fig. 5a at T = 95.8. The cavity is now deeper than it is wide and the external flow is seen not to penetrate the cavity. Instead, a rather weak recirculating eddy occupies most of the cavity volume. In addition much weaker eddies develop in the undercut regions, and transport in these regions can be thought of as occurring mainly by diffusion. Since transport in the undercut regions is less efficient than in the rest of the cavity, better etch anisotropy is obtained as compared to pure diffusion, as already mentioned above. However, for deep cavities this advantage is lost because fluid flow is very weak deeper in the cavity. The advantage is regained if some means is devised to enhance fluid flow within the cavity, even for deep cavities. Kuiken and Tijburg (4) made use of free convection phenomena to achieve this goal. The key is to disrupt the "boundary layer" at the cavity mouth which prevents efficient communication of the external flow with the flow within the deep cavity.

Returning to the profiles shown in Fig. 5a, at early times when the cavity aspect ratio is close to 1:4, the external flow invades the bottom of the cavity bringing fresh reagent in the cavity. The etch rate is then higher around the area where the fluid first encounters the bottom of the cavity (i.e., around position X = -0.2, see also Fig. 5b and 6a). At later times when a large eddy almost fills the cavity, fresh reactant first reaches the area around the right mask edge, resulting in higher etch rate there and faster mask undercut. Figure 7 shows a concentration contour plot for the cavity corresponding to T = 95.8 in Fig. 5a. One observes larger concentrations around the right mask edge as
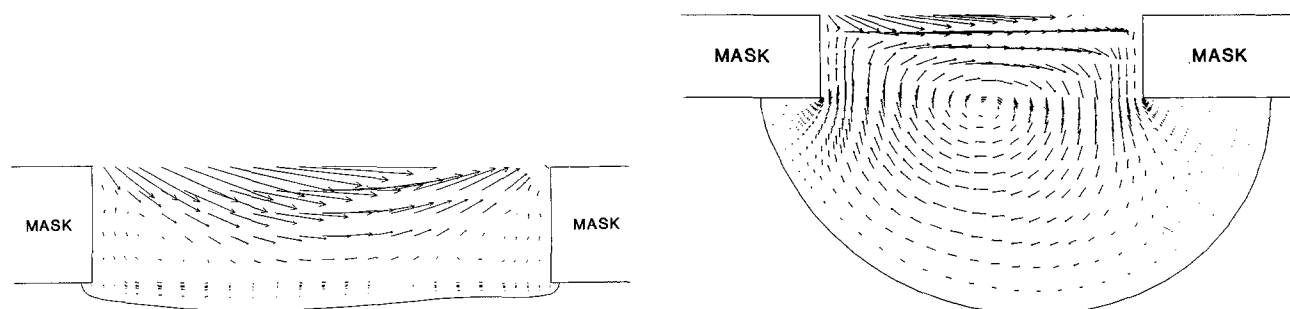

Fig. 6. (a, left) Velocity vector plot in the cavity corresponding to T = 4.0 of Fig. 5a. (b, right) Velocity vector plot in the cavity corresponding to T = 95.8 of Fig. 5a.
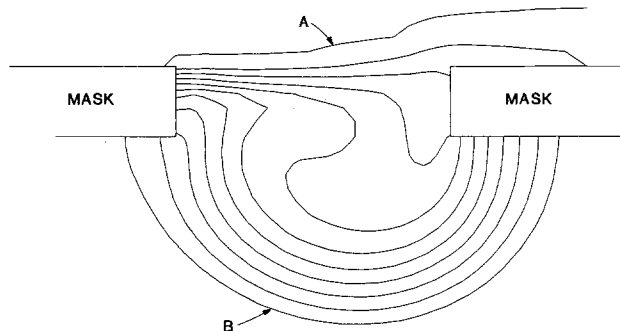
Fig. 7. Concentration contour plot in the cavity corresponding to $T = 95.8$ of Fig. 5a. Contour named A corresponds to dimensionless concentration $C = 0.99$. Contour B (wall of cavity) corresponds to $C = 0$. Linear interpolation applies for the in-between contours.

compared to the left mask. Moreover, the concentration gradients are higher in places where the contours are closer together. One observes larger concentration gradients in the undercut area of the right mask as compared to the left mask. This implies higher rate of undercutting of the right mask in agreement with the discussion above.

At lower Peclet numbers, both the etch rate and the etch factor were reduced, and the etch profiles were less asymmetric. Such behavior is to be expected since lowering of Pe is tantamount to decreasing the level of convection. In fact, for very small Pe the situation is essentially identical to that of pure diffusion.

Figure 8a shows the shape evolution of a cavity under conditions identical to those of Fig. 5 except that the surface reaction had a finite speed ($\Phi = 1$ instead of $\Phi \rightarrow \infty$). In the presence of surface reaction kinetic limitations, the etch rate distribution along the reacting surface is expected to be more uniform as compared to the diffusion-controlled case of Fig. 5. Hence the etch profiles shown in Fig. 8 are less asymmetric compared to the profiles of Fig. 5. In addition the etch rate is lower and the etch anisotropy (etch factor) is lesser. In the limit of surface reaction kinetic control ($\Phi \rightarrow 0$), the etch rate will be uniform along the reacting surface and independent of the cavity depth. In such case, the etch factor will be unity. Obviously, the kinetically controlled etching case is not favorable in terms of throughput and anisotropy. Figure 8b is a concentration contour plot corresponding to the profile at $T = 96.3$ of Fig. 8a. In contrast to the diffusion-controlled case (Fig. 7), the reactant concentration is not constant along the etching surface (in Fig. 7 the surface concentration is zero). An inspection of the concentration distribution along the etching surface gives an idea of the etch rate distribution, since the etch rate is proportional to the surface concentration. The undercut of the right mask is again higher as compared to that of the left mask but the difference is not as large as in the diffusion-controlled case.

Results on etch rate and etch factor are summarized in Fig. 9 and 10, respectively. The etch rate shown in Fig. 9 was calculated by dividing the etched depth at $X = 0$ by the corresponding elapsed time T. Therefore this is a "time-average" etch rate in contrast to the instantaneous

Fig. 9. Etch rate at $X = 0$ as a function of the cumulative time for cavities etching under the conditions of Fig. 3a (curve I), Fig. 4a (curve II), and Fig. 5a (curve III).

Fig. 10. Etch factor as a function of cumulative time for cavities etching under the conditions of Fig. 3a (curve I), Fig. 4a (curve II), and Fig. 5a (curve III).

etch rate which is proportional to the flux (Fig. 3b, 4b, and 5b). In the case of pure diffusion (curves I and II), the etch rate is infinite at $T = 0$ and decreases monotonically with
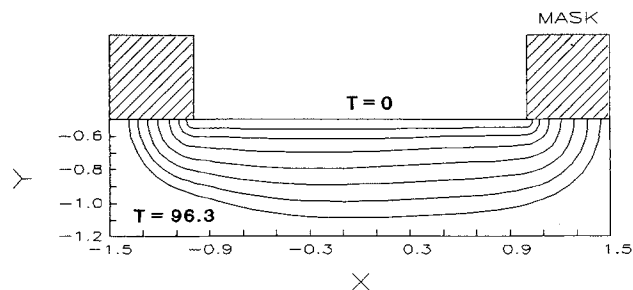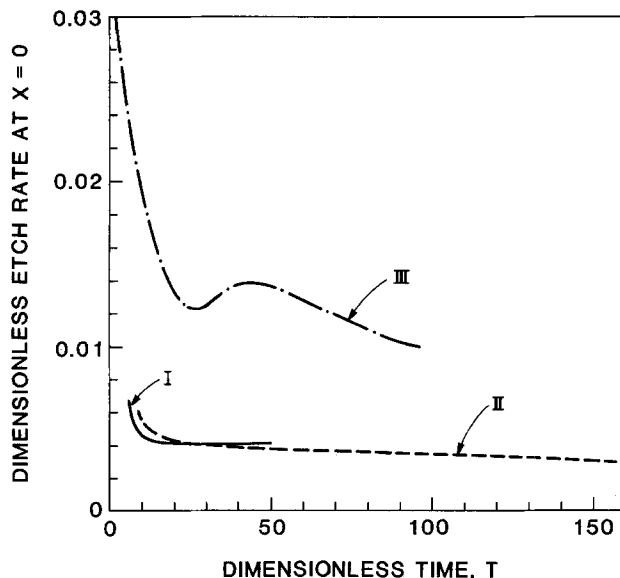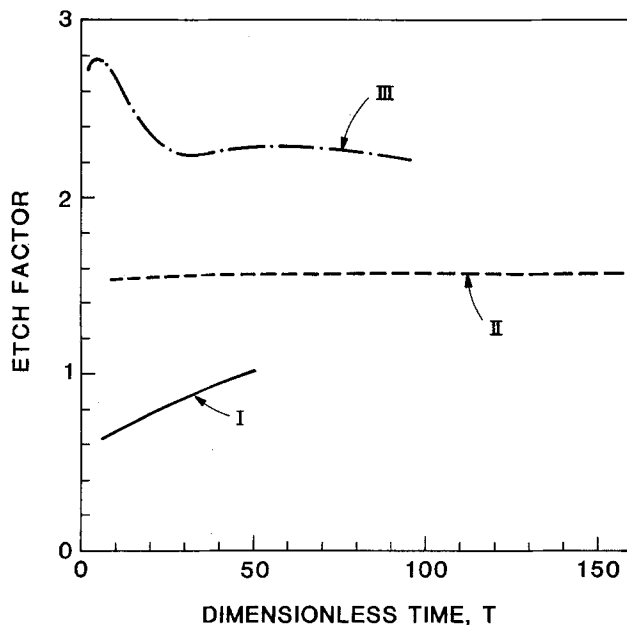

Fig. 8. (a, left) Shape evolution of a cavity under fluid flow conditions and with $\Phi = 1$. Other conditions were as in Fig. 5a. Cavity wall profiles are shown for dimensionless times $T = 0, 7.6, 15.8, 27.4, 43.1, 60.5, 78.6,$ and 96.3. (b, right) Concentration contour plot in the cavity corresponding to $T = 96.3$ of Fig. 8a. Contour named A corresponds to dimensionless concentration of 0.99. Contour K corresponds to dimensionless concentration of 0.31. Linear interpolation applies for the in-between contours.

time. In the case of fluid flow (curve III), the etch rate is substantially higher especially at the early times. The local maximum in etch rate at about T = 40 is associated with the change in flow patterns in the cavity as the cavity aspect ratio increases (see discussion above). The etch rate in the case of fluid flow depends strongly on time, which in turn reflects a dependence of the etch rate on the cavity aspect ratio. This fact has important practical implications; cavities of different aspect ratio may be etching at very different rates. For example, for the same mask thickness, cavities with smaller mouthwidth will be etching slower if diffusional limitations play a role in the etching process.

The etch factor in Fig. 10 was calculated by dividing the etched depth at $X = 0$ by the mask undercut. For the case of fluid flow, for which the etch profiles were not symmetric, an arithmetic average of the left and right mask undercut was used. For pure diffusion, one observes a significantly higher etch factor with a mask of finite thickness (curve II) as compared to the infinitely thin mask (curve I), especially at the early times. Fluid flow enhances the etch factor even further, especially at the early times when the external flow penetrates the cavity. Under the flow conditions examined, the etch factor varied between 2 and 3. In addition, the etch factor quickly decreased with time at early times, but became insensitive to time at later times. These results are in qualitative agreement with the experimental observations of Allen *et al.* (20). Unfortunately not enough information is provided by Allen and co-workers to allow for a direct quantitative comparison with the present model predictions.

Summary and Conclusions

A general purpose mathematical procedure was developed to study the shape evolution of two-dimensional cavities during wet chemical etching under the influence of fluid flow. Finite element methods were employed to solve for the fluid velocity profiles and for the reactant concentration distribution in cavities of arbitrary shape. In particular, the Streamline Upwind/Petrov Galerkin (SU/PG) finite element method was used for the convective-diffusion equation since this method is better suited for convection-dominated flows (high Peclet numbers), such as the case studied. A moving boundary scheme was developed to track the shape evolution of the cavity. The mathematical procedure was applied to the problem of wet chemical etching of two-dimensional cavities under cross flow conditions. The simplified case of etching in a quiescent solution (no fluid flow) was examined as well.

When etching in a quiescent solution under conditions of diffusion control, a characteristic bulging of the wall profiles appeared close to the mask edge, at the early stages of etching. This bulging was especially pronounced for an infinitely thin mask but the bulging was much weaker for a realistic mask having thickness 1/4 of the cavity mouthwidth. In addition, the thicker mask resulted in significantly better etch anisotropy with only slightly different etch rate.

With fluid flow across the cavity, the time-averaged etch rate increased four times and the time-averaged etch factor increased by 40% as compared to pure diffusion, under the conditions studied. The etch rate and etch factor were found to depend strongly on the cavity aspect ratio, degrading as the cavity became deeper. Furthermore, the etch profiles showed a strong dependence on the etching time. At early times, when the cavity aspect ratio was smaller than 1:3, etching was faster to the left of the cavity centerline (fluid was entering from the left). As etching proceeded, and the cavity depth increased with a concomitant increase in the cavity aspect ratio, etching rate was faster to the right of the centerline. The above phenomena were explained by considering the hydrodynamic flow patterns in the cavity as the cavity aspect ratio increased during etching.

The problem studied is only a simplified case of a real etching system. Thus, solution chemistry, complex surface reaction kinetics, gas evolution, the presence of surface films, or of crystallographic effects were not considered. In addition a simple shear flow was assumed past

the cavity. However, some of the salient features of the process were revealed by studying the simplified case. Moreover, the numerical code can be expanded to study different flow configurations (such as impinging jet flow), free convection phenomena, complicated reaction sequences, and the effect of laser illumination of the etching surface.

In mass-transfer controlled situations, the etch profile of a microscopic cavity depends in a complex manner on the time-varying multidimensional fluid velocity and concentration fields. Prediction of the etch rate and mask undercut under a variety of etching conditions is then difficult to make based on intuition alone. Powerful mathematical techniques based on the finite element method can be used to quantitatively analyze the complex interaction of transport and reaction phenomena and their effect on the shape evolution of the cavity. Comparison with experimental data under well-characterized conditions would greatly add to the usefulness of the mathematical model. The model may then be used to identify operating conditions that result in high rate anisotropic etching.

LIST OF SYMBOLS

B	dimensionless parameter (Eq. [35])
c	reactant concentration, mols/cm^3
C	dimensionless reactant concentration (Eq. [14])
D	reactant diffusivity, cm^2/s
h	mask thickness, cm
k	surface reaction rate constant, cm/s
L	half-width of cavity mouth, cm
M_s	molecular weight of solid, g/mol
m	stoichiometric coefficient in etching reaction (Eq. [12])
n	outward unit normal vector
p	pressure, dynes/cm^2
P	dimensionless pressure (Eq. 14)
Pe	Peclet number, dimensionless (Eq. 15)
Re	Reynolds number, dimensionless (Eq. 15)
t	time, s
T	dimensionless time (Eq. [35])
U	dimensionless fluid velocity (Eq. [13])
u_c	fluid velocity at center of cavity mouth, cm/s
v_n	velocity of moving boundary along the outward normal, cm/s
V_n	dimensionless velocity of the moving boundary along the outward normal for the case of fluid flow
V_n^*	dimensionless velocity of the moving boundary along the outward normal for the case of pure diffusion

Greek

β	dimensionless parameter (Eq. [16])
Γ_i	boundary surface ($i = 1, 2, \ldots, 6$), Fig. 1
μ	fluid viscosity, poise
ν	fluid kinematic viscocity, cm^2/s
ρ_s	solid density, g/cm^3
σ	parameter (Eq. [11])
τ	dimensionless time (Eq. [14])
Φ	Thiele modulus (Eq. [16])
Ω	computational domain, Fig. 1

Subscript

o	signifies initial condition

Superscript

n	signifies the nth time step

REFERENCES

1. "Thin Film Processes," J. L. Vossen and W. Kern, Editors, Academic Press, Inc., New York (1978).
2. S. K. Ghandhi, "VLSI Fabrication Principles," John Wiley & Sons, Inc., New York (1983).

3. G. Kaminsky, *J. Vac. Sci. Technol.*, **B3**, 1015 (1985).
4. H. K. Kuiken and R. P. Tijburg, *This Journal*, **130**, 1722 (1983).
5. R. Alkire and H. Deligianni, *ibid.*, **135**, 1093 (1988).
6. D. V. Podlesnik, H. H. Gilgen, A. E. Willner, and R. M. Osgood, Jr., *J. Opt. Soc. Am. B*, **3**, 775 (1986); M. M. Carrabba, N. M. Nguyen, and R. D. Rauh, *This Journal*, **134**, 1855 (1987).
7. C. Vuik and C. Cuvelier, *J. Comput. Physics*, **59**, 247 (1985).
8. H. K. Kuiken, *Proc. R. Soc. London, Ser. A*, **396**, 95 (1984).
9. H. K. Kuiken, *ibid.*, **392**, 199 (1984).
10. H. K. Kuiken, J. J. Kelly, and P. H. L. Notten, *This Journal*, **133**, 1217 (1986).
11. R. C. Alkire, D. B. Reiser, and R. L. Sani, *ibid.*, **131**, 2795 (1984).
12. E. C. Hume, W. M. Deen, and R. A. Brown, *ibid.*, **131**, 1251 (1984).
13. P. H. L. Notten, J. J. Kelly, and H. K. Kuiken, *ibid.*, **133** 1226 (1986).
14. T. J. R. Hughes, W. K. Liu, and A. Brooks, *J. Comput. Phys.*, **30**, 1 (1979).
15. A. N. Brooks and T. J. R. Hughes, *Comp. Methods Appl. Mech. Eng.*, **32**, 199 (1982).
16. T. E. Tezduyar and Y. J. Park, *ibid.*, **59**, 307 (1986).
17. R. Glowinski, "Numerical Methods for Nonlinear Variational Problems," Springer-Verlag, New York (1984).
18. P. Murray and G. F. Carey, *J. Comp. Phys.*, **74**, 440 (1988).
19. J. J. L. Higdon, *J. Fluid Mech.*, **159**, 195 (1985).
20. D. M. Allen, D. F. Horne, and G. W. W. Stevens, *J. Photog. Sci.*, **27**, 181 (1979).

A Photoelectron Spectroscopy Study of CF$_4$/H$_2$ Reactive Ion Etching Residue on Tantalum Disilicide

J. H. Thomas, III* and L. H. Hammer

David Sarnoff Research Center, Princeton, New Jersey 08543

ABSTRACT

X-ray photoelectron spectroscopy has been used to characterize CF$_4$/30% H$_2$ reactive ion etching residue on the tantalum disilicide surface after removing 100 nm of silicon dioxide. This was done to simulate the structure of multilevel metallization presently being encountered in integrated circuit manufacture. At a pressure of 80 millitorr and a power density of 1 W/cm^2, the residue layer formed consists chemically of a mixed tantalum and silicon fluoride and oxide-like film. This layer is complex and does not appear to contain polymeric fluorocarbon as has been observed on silicon at slightly higher hydrogen concentrations in the glow discharge. Its thickness is estimated to be 3 nm based on electron escape depths. The presence of SiO$_2$ causes the surface residue layer to be more oxygen rich in comparison with the uncoated tantalum disilicide surface. Sputtering does occur at a self-bias of 300V and results in preferentially removing silicon. Core-level binding energies are reported for tantalum disilicide, the etch residue, the native oxide on the disilicide, and some related materials for reference purposes.

Multilevel metallization used in submicrometer integrated circuit manufacture requires that ohmic contact be made to the first level metallization after reactive ion etching contact vias through deposited insulator layers such as silicon dioxide (1). Refractory metal silicides are presently being used in process technologies such as the "polycide" process (2-4). The polycide process consists of a conductive silicide deposited on polysilicon that is used in gate metallization. For gate metallization, conductive silicides on polysilicon incorporate the best features of a polysilicon gate contact along with the low resistivity of the silicide to reduce series resistances encountered in submicrometer dimension interconnects (2, 3). Consequently, this metallization can be used the first level of a multilevel metallized device structure.

One possibility for first level metallization of high submicrometer reliability devices is tantalum disilicide (2-5). Tantalum disilicide is readily compatable with standard circuit processing using common plasma or reactive ion etching processes. Tantalum silicide behaves as a metallic conductor with a room temperature resistivity of around 40 μΩ-cm after appropriate thermal annealing to form the stoichiometric silicide (5-8).

Multilevel metallization requires that contacts between metallization levels be made through submicrometer dimension vias etched in an insulating isolation layer such as silicon dioxide. The etching process, typically reactive ion etching in the presence of a photoresist mask, leaves a residue on the metal surface to which the contact is being made (9-12). As in contacts to silicon (13, 14), this residue layer adds to the series electrical resistance of the contact and causes degradation of the high-frequency operation of the circuit. It is, therefore, important to characterize these processing residues and determine their origin so that pro-

cesses can be included or modified to eliminate (or reduce) the surface residue layers.

In this study, silicon dioxide coated tantalum disilicide was reactive ion etched in a small scale plasma chamber attached to an x-ray photoemission spectroscopy (XPS) system. Fluorocarbon reactive ion etching (in this study, CF$_4$/30% H$_2$ was used), commonly encountered in silicon dioxide etching and patterning, was used to etch silicon dioxide off of the tantalum disilicide surface. The surface residue layer was studied *in situ* using x-ray photoemission and was compared with other thin surface layers on related materials. Core-level binding energies for tantalum disilicide, its native oxide, the plasma induced residue layer and the effects of atmospheric exposure on the residue layer are reported. The effect of the presence of SiO$_2$ on the chemistry of the residue layer is discussed.

Experimental

Tantalum silicide was deposited on polysilicon on silicon-on-sapphire wafers by cosputtering from a tantalum rich target in a Varian 3180 system to a thickness of 200 nm. The tantalum-rich deposit was annealed at approximately 900°C for 30 min in argon atmosphere. The stoichiometry and film thickness were determined by Rutherford backscattering spectrometry in our laboratory. Films were shown to be stoichiometric tantalum disilicide within experimental error. Two wafers were selected from the batch of processed and annealed wafers. Silicon dioxide was then chemical vapor deposited to a thickness of 100 nm on the tantalum disilicide surface to simulate a typical double level metallization scheme. Etching of contact vias was simulated by etching the silicon dioxide to the tantalum disilicide surface using a fluorocarbon reactive ion etching process. A 60% overetch was provided to assure complete oxide removal. The uncoated tantalum di-